Relationship Between Stagnation Point Deflection and Forebody Vortex Asymmetry

L. A. Darden* and N. M. Komerath†
Georgia Institute of Technology, Atlanta, Georgia 30332-0150

Introduction

WHEN the angle of attack exceeds the included angle[1] of a vehicle nose tip, the leeside vortices over the forebody generally become asymmetric. This asymmetry causes a side force, yawing moment, and rolling moment that are large enough to saturate flight controls, even with thrust vectoring,[2] and has been difficult to eliminate. We have previously shown steady-state correction of asymmetry by making minor modifications to the nose tip stagnation point on a double-delta wing-body model with a pointed nose.[3] In this Note, the asymmetry in the cross flow on a wing body at angle of attack is shown to be a deterministic phenomenon, linearly related to the displacement of the nose tip stagnation point. Continuous control of asymmetry is shown using a stagnation point actuator (SPA), which displaces the nose tip stagnation point in the yaw plane, as shown in Fig. 1. The response of this asymmetry to stagnation point displacement is studied using frequency-domain analysis of position data obtained from video images of the flow and the SPA deflection.

Control techniques in the previous literature focus on controlling the vortices after they are developed, using steady or pulsed binary blowing[4] or high-frequency alternating suction and blowing[5] from the forebody surface and strakes[6] or rotating an elliptic nose[7,8] about the longitudinal axis so that the surface geometry and discontinuities in slope are modified. Numerical simulations of asymmetry based on stability analyses[9] have indicated that microasymmetries generated in the flow upstream of the model have the same effect as microasymmetries on the forebody surface and would be felt downstream at convection speed. Flight results might reinforce this theory: identical aircraft have shown markedly different yawing moment characteristics.[2] None of the preceding techniques actually alters the stagnation point location, which is at the nose tip on a sharp-nosed forebody. Most techniques have only studied isolated forebodies at low Reynolds number. They have achieved quasisteady and binary control of asymmetry over specific ranges of test conditions by tailoring the rotation schedule of the elliptic cross section[8] or by modifying the flow rate[5] or the duty cycle[6] of the pulsed pneumatics. Discontinuities[8] and adverse effects under yaw[6] were encountered. The dynamic response of the asymmetry has not been studied.

Approach

In this Note, the asymmetry in the vortex patterns in a cross-flow plane near the wing-body juncture (Fig. 1) is related to the stagnation point displacement. For the first time, the time scale of this response is captured. This is done by analyzing digitized video images of the SPA motion and the asymmetry in the vortex pattern and constructing a time series spanning several seconds. The resulting time series is sampled, transformed to the frequency domain, and analyzed by standard methods in digital signal processing to compute the autospectra, the cross spectrum, the coherence function, and the complex transfer function. The autospectrum shows the distribution of fluctuation energy over the range of frequencies of interest. The cross spectrum captures the fluctuation energy common to the input (the SPA motion) and the output (the vortex asymmetry) as a function of frequency. The coherence shows the extent of the causal linear relationship existing between the SPA motion and the asymmetry in each frequency interval. In intervals where the coherence function is near unity, the values of the transfer function are reliable. The transfer function magnitude gives the sensitivity of the asymmetry to SPA motion as a function of frequency. The phase variation with frequency indicates the time lag between asymmetry and SPA motion.

Vortex asymmetry is manifested in both the strengths and trajectories of the two forebody vortices. A single metric of asymmetry is needed to develop a relationship between SPA displacement and vortex asymmetry in the flowfield. Figure 1 shows the concept of the zero vorticity contour (ZVC), which is clearly visible in cross-flow light sheet images of smoke patterns around the vortices. Along a thin layer between the vortices, the induced velocities due to the two vortices result in a purely potential, straight, jet-like flow. The centerline of this flow region is a line where the component of vorticity perpendicular to the plane of the image is zero: this line is called the ZVC. Extrapolating this straight line to the surface contour of the body gives an intersection point whose azimuth can be measured, relative to the plane of lateral symmetry. Note that this is not a stagnation point; in fact, the velocity at the ZVC is quite high. This azimuth is used as the metric of asymmetry. It can be located accurately by combining patience and judgment with the precision of a 640 × 480 pixel image of the cross-flow plane, with a laser sheet illuminating the smoke crossing the plane. This measure of asymmetry is based on the potential flow away from the surface.

The AR2Δ wing body (Fig. 1) has a delta wing of aspect ratio 2 with leading edges beveled at 18 deg on the lower surface, a 50-mm-diam cylindrical fuselage, and a body-of-revolution forebody, covered at the tip with a cone of apex half-angle 15 deg. The cone is yawed using a push rod connected to a servo motor inside the fuselage. In this experiment, the servo motor was driven using a human-operated radio control lever. The maximum yaw of 13 deg corresponded to 7.14-mm displacement of the apex from the plane of symmetry. Given the sharpness of the tip, it is safely assumed that the stagnation point remains negligibly displaced from the geometric apex of the cone. The nose tip position was measured by videotaping the shadow of the nose tip in a flashlight beam cast on a grid on the tunnel wall. This was calibrated using a digital inclinometer. Following tests where quasistatic correction of asymmetry was achieved at $\alpha \leq 50$ deg,[10] the model was mounted at angle of attack $\alpha = 30$ deg in a 1.07 × 1.07 m wind tunnel. The wind speed of 2.1 m/s gives a Reynolds number based on fuselage diameter of 7.3×10^3. Details are given in Ref. 10.

Smoke from wax-coated wires was illuminated in the selected cross-flow plane using a sheet from a 3-W argon ion laser. A downstream video camera recorded the patterns. The tapes of the vortex pattern and the nose tip motion were synchronized to ±0.0085 s by counting frames from the frame where the flashlight first came on. Plane A is 0.336 L downstream of the nose tip, where the total model length L is 0.7716 m. This shows the forebody and wing leading-edge vortices slightly downstream of the wing-body juncture. Plane B is over the wings, 63.5 mm downstream of plane A.

From the video data at plane A, 370 digitized images of the vortex flow and the same number of the SPA were analyzed. In each image the intersection of the ZVC with the model surface was tracked. Images of a recorded grid were used to calibrate size and correct for distortions. The first 206 time steps of the SPA and the ZVC are shown in Fig. 2. Every point comes from a different image. The uncertainty in measurement is less than 1 deg, as seen in the SPA signal, where there is no random motion. The ±5-deg noise in the ZVC signal is attributed to the uncertainty in smoke entrainment and flow unsteadiness; this is why statistical analysis is needed to quantify the asymmetry. The sudden movements of the SPA are rich in frequency content. The ZVC response is also step-like but with a complex phase relationship. The two time series were sampled every $\frac{1}{30}$ s for 6.86 s. To remove phase bias, a random number generator determined the starting point for each 128-point sample within the digital record. Autospectra[11] of the nose and ZVC motion and their cross spectrum[11] were computed with a frequency resolution of 0.234 Hz. Averages of 1000 iterations are presented.

Presented as Paper 95-1775 at the AIAA 13th Applied Aerodynamics Conference, San Diego, CA, June 19–22, 1995; received Sept. 3, 1996; revision received July 21, 1997; accepted for publication July 28, 1997. Copyright © 1997 by L. A. Darden and N. M. Komerath. Published by the American Institute of Aeronautics and Astronautics, Inc., with permission.

*Ph.D. Candidate, School of Aerospace Engineering. Student Member AIAA.

†Professor, School of Aerospace Engineering. Associate Fellow AIAA.

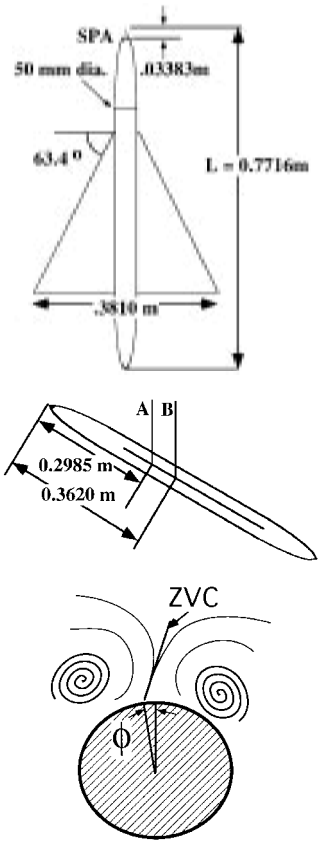

Fig. 1 AR2Δ wing-body model with SPA at the tip and measurement planes A and B. Schematic sketch of cross-flow pattern shows the ZVC.

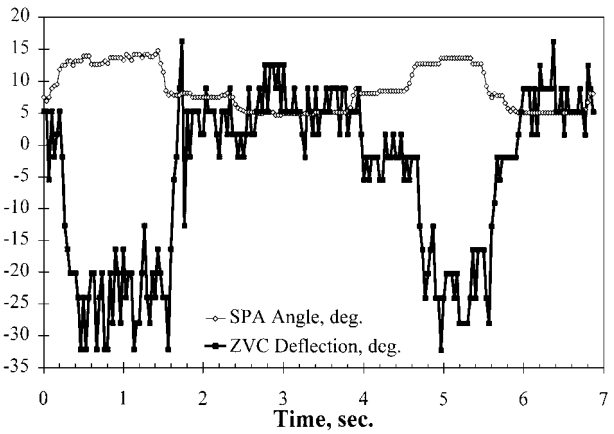

Fig. 2 Time series measured from video images of nose deflection and the simultaneous vortex asymmetry at plane A.

Figure 3a shows autospectra of the SPA motion and the ZVC response at plane A. The spectral energy peaks at about 0.4 Hz, the reciprocal of the approximate interval between movements of the control lever. At plane A, every frame was analyzed, giving a Nyquist frequency of 15 Hz. Figure 3b shows coherence of >0.9 at frequencies where signal energy is significant. In this range, it is justifiable to determine a transfer function. The magnitude of the transfer function is roughly constant over frequency, as seen in the rolling moment in Refs. 12 and 13. Figure 3b also shows the transfer function phase. The 180-deg phase at the steady-state limit is because SPA movement to the right moves the ZVC left and vice versa.

A linear fit to the phase variation at points of high coherence and spectral level yields a time delay of 0.102 s, compared with the 0.125-s lag (τ_∞) for convection at U_∞, along the body axis. At plane B, τ_∞ is 0.153 s. Counting video frames from the first nose motion to the first ZVC response yields 0.133 s at plane A and 0.2 s at plane B. The long delays seen in Ref. 10 were traced to an intermittent malfunction of the recording time-code generator, which caused the

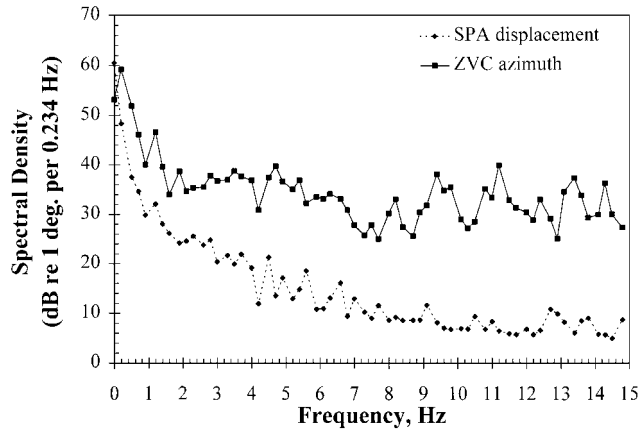

Fig. 3a Autospectra of nose motion and vortex response at plane A.

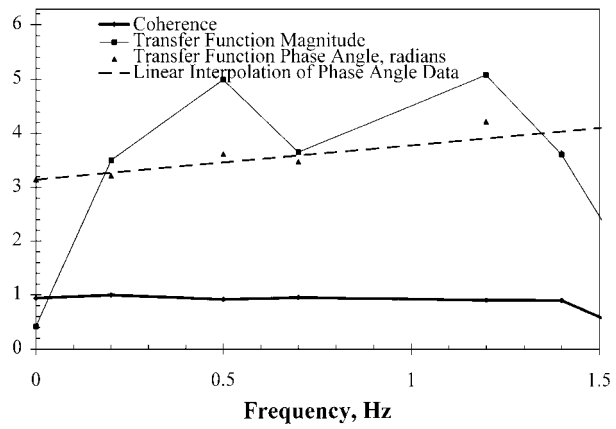

Fig. 3b Coherence, magnitude, and phase of the transfer function between nose motion and vortex response at plane A.

first vortex response to be ignored as noncausal. For the present results, the time series were confirmed against an external clock.

We have shown continous control of forebody vortex asymmetry, both in a quasisteady manner and at fairly high rates, in Refs. 10, 12, and 13. This has succeeded over the range $25 \leq \alpha \leq 45$ deg. A linear causal relationship is verified here between the nose motion and the vortex response. The response of the asymmetry as gauged from the potential flow occurs essentially at the quickest convective speed in the flow. This point should be noted in view of the results of Refs. 12 and 13 showing delays in the surface pressure and wing rolling moment development, exceeding the convection time by an order of magnitude.

Conclusions

The following conclusions are drawn.

1) Lateral vortex asymmetry at high angle of attack is controlled by deflecting the nose tip stagnation point, both statically and dynamically.

2) The surface intersection of the ZVC is causally and linearly related to the movement of the nose tip stagnation point.

3) The time lag in vortex asymmetry response as seen from the flow images occurs at approximately freestream convection speed.

Acknowledgments

This work was performed under Air Force Office of Scientific Research Grant F49620-93-1-0342, monitored by Daniel Fant. The first author received support from a National Science Foundation graduate fellowship. Assistance from the Experimental Aerodynamics Group is gratefully acknowledged.

References

[1]Ericsson, L. E., and Reding, J. P., "Asymmetric Vortex Shedding from Bodies of Revolution," *Tactical Missile Aerodynamics*, Vol. 104, 1986, pp. 243–296.

[2]Cobleigh, B. R., "High-Angle-of-Attack Yawing Moment Asymmetry of the X-31 Aircraft from Flight Test," NASA CR 186030, Sept. 1994.

[3]Komerath, N. M., Liou, S.-G., DeBry, B., and Lenakos, J., "Measurements of the Unsteady Vortex Flow over a Wing-Body at Angle of Attack," AIAA Paper 92-2729, June 1992.

[4]Lee, R., Hanff, E. S., and Kind, R. J., "Wind-Tunnel Investigation of Dynamic Manipulation of Forebody Vortices," AIAA Paper 95-1794, June 1995.

[5]Williams, D., and Bernhardt, J., "Proportional Control of Asymmetric Forebody Vortices with the Unsteady Bleed Technique," AIAA Paper 90-1629, June 1990.

[6]Malcolm, G. N., "Forebody Vortex Control," AGARD Rept. 776, March 1991, pp. 1-6–40.

[7]Moskovitz, C., Hall, R., and Dejarnette, F., "Experimental Investigation of a New Device to Control the Asymmetric Flowfield on Forebodies at Large Angles of Attack," AIAA Paper 90-0068, Jan. 1990.

[8]Bridges, D. H., and Hornung, H. G., "Elliptic Tip Effects on the Vortex Wake of an Axisymmetric Body at Incidence," *AIAA Journal*, Vol. 32, No. 7, 1992, pp. 1437–1445.

[9]Degani, D., and Tobak, M., "Numerical Simulation of Upstream Disturbance on Flows Around a Slender Body," AIAA Paper 93-2956, June 1993.

[10]Darden, L. A., and Komerath, N. M., "Forebody Vortex Control at High Incidence Using a Moveable Nose Stagnation Point," AIAA Paper 95-1775, June 1995.

[11]Bendat, J. S., and Piersol, A. G., *Random Data Analysis and Measurement Procedures*, 2nd ed., Wiley, New York, 1986, Chaps. 5, 6.

[12]Darden, L. A., Peterson, K. G., and Komerath, N. M., "Vortex Control Using a Moveable Nose with Pressure Feedback," AIAA Paper 95-3468, Aug. 1995.

[13]Peterson, K. G., Darden, L. A., and Komerath, N. M., "Dynamic Roll Control Experiments Using a Moveable Nosetip," AIAA Paper 96-0789, Jan. 1996.

A. Plotkin
Associate Editor

Piezoelectric Constitutive Equations for a Plate Shape Sensor/Actuator

Shengyuan Yang* and Wenhao Huang†
University of Science and Technology of China, Hefei, Anhui 230026, People's Republic of China

Introduction

USING piezoelectric sensors and actuators for monitoring and controlling the motion of a flexible structure has been widely discussed during the past few decades.[1,2] The flexible structures concerned are laminated plates, and then the piezoelectric sensors and actuators used are of plate shape. Therefore, when one analyzes and simulates the mechanical and electrical motions of a structure based on the classical laminate plate theory, the plane form of the general piezoelectric constitutive equations, i.e., the piezoelectric constitutive equations of a plate shape sensor or actuator, should be adopted. In fact, related previous reports have attempted to do so.[3–6] However, in previous reports the plane form piezoelectric constitutive equations are only written in forms. The relationships between the plane form piezoelectric constitutive equations and the general piezoelectric constitutive equations have not been shown. These relationships, according to which the constants in the plane form equations can be obtained from the manufacturer-given constants in the general equations, are necessary and important when one carries out analysis of laminated piezoelectric plates. In this Note, from the general piezoelectric constitutive equations and based on the Kirchhoff hypothesis of the classical laminate plate theory, we will derive the piezoelectric constitutive equations of a plate shape sensor or actuator.

Received May 16, 1997; revision received July 21, 1997; accepted for publication July 24, 1997. Copyright © 1997 by the American Institute of Aeronautics and Astronautics, Inc. All rights reserved.

*Ph.D. Student, Department of Precision Machinery and Precision Instrumentation.

†Professor, Department of Precision Machinery and Precision Instrumentation.

Equations

The commonly named piezoelectric constitutive equations, i.e., the so-called general piezoelectric constitutive equations in this Note, can be written as[7]

$$D_i = e_{ij} S_j + \varepsilon_{ik}^S E_k \tag{1a}$$

$$T_l = c_{lj}^E S_j - e_{kl} E_k \tag{1b}$$

where $i, k = 1, 2, 3$ and $j, l = 1, 2, 3, 4, 5, 6$; D_i and E_k represent the electric field and electric displacement, respectively; S_j and T_l represent strain and stress, respectively; e_{ij} represents the piezoelectric stress/charge matrix, ε_{ik}^S represents the permitivity matrix measured at constant strain, and c_{lj}^E represents the elastic stiffness matrix measured at constant electric field.

Usually, the thickness direction of a plate shape sensor or actuator is designated by direction 3. Its two surfaces that are parallel to the plate plane are the two electrodes. In classical laminate plate theory, the Kirchhoff hypothesis is adopted.[8] That is, T_3 can be neglected relative to T_1 and T_2; any line perpendicular to the plate midplane before deformation remains perpendicular to the midplane after deformation; then there are no shear strains in any plane perpendicular to the plate midplane. The result is

$$T_3 = 0, \qquad S_4 = S_5 = 0 \tag{2}$$

Substituting Eq. (2) into Eq. (1b), we can obtain

$$T_1 = c_{11}^E S_1 + c_{12}^E S_2 + c_{13}^E S_3 + c_{16}^E S_6 - e_{11} E_1 - e_{21} E_2 - e_{31} E_3 \tag{3a}$$

$$T_2 = c_{12}^E S_1 + c_{22}^E S_2 + c_{23}^E S_3 + c_{26}^E S_6 - e_{12} E_1 - e_{22} E_2 - e_{32} E_3 \tag{3b}$$

$$0 = c_{13}^E S_1 + c_{23}^E S_2 + c_{33}^E S_3 + c_{36}^E S_6 - e_{13} E_1 - e_{23} E_2 - e_{33} E_3 \tag{3c}$$

$$T_6 = c_{16}^E S_1 + c_{26}^E S_2 + c_{36}^E S_3 + c_{66}^E S_6 - e_{16} E_1 - e_{26} E_2 - e_{36} E_3 \tag{3d}$$

According to Eq. (3c), we get

$$S_3 = -\frac{c_{13}^E S_1 + c_{23}^E S_2 + c_{36}^E S_6 - e_{13} E_1 - e_{23} E_2 - e_{33} E_3}{c_{33}^E} \tag{4}$$

Substituting Eq. (4) into Eqs. (3a), (3b), and (3d) we get

$$\begin{aligned}
T_1 &= \left[c_{11}^E - \left(c_{13}^E\right)^2 / c_{33}^E\right] S_1 + \left(c_{12}^E - c_{13}^E c_{23}^E / c_{33}^E\right) S_2 \\
&\quad + \left(c_{16}^E - c_{13}^E c_{36}^E / c_{33}^E\right) S_6 - \left(e_{11} - e_{13} c_{13}^E / c_{33}^E\right) E_1 \\
&\quad - \left(e_{21} - e_{23} c_{13}^E / c_{33}^E\right) E_2 - \left(e_{31} - e_{33} c_{13}^E / c_{33}^E\right) E_3 \\
T_2 &= \left(c_{12}^E - c_{13}^E c_{23}^E / c_{33}^E\right) S_1 + \left[c_{22}^E - \left(c_{23}^E\right)^2 / c_{33}^E\right] S_2 \\
&\quad + \left(c_{26}^E - c_{23}^E c_{36}^E / c_{33}^E\right) S_6 - \left(e_{12} - e_{13} c_{23}^E / c_{33}^E\right) E_1 \\
&\quad - \left(e_{22} - e_{23} c_{23}^E / c_{33}^E\right) E_2 - \left(e_{32} - e_{33} c_{23}^E / c_{33}^E\right) E_3 \\
T_6 &= \left(c_{16}^E - c_{13}^E c_{36}^E / c_{33}^E\right) S_1 + \left(c_{26}^E - c_{23}^E c_{36}^E / c_{33}^E\right) S_2 \\
&\quad + \left[c_{66}^E - \left(c_{36}^E\right)^2 / c_{33}^E\right] S_6 - \left(e_{16} - e_{13} c_{36}^E / c_{33}^E\right) E_1 \\
&\quad - \left(e_{26} - e_{23} c_{36}^E / c_{33}^E\right) E_2 - \left(e_{36} - e_{33} c_{23}^E / c_{36}^E\right) E_3
\end{aligned} \tag{5}$$